Incomplete Fusion Defects and Deformation Behavior in GMA-DED of 316L and 316LSi

The influence of hatch spacing on tensile properties of high deposition rate gas metal arc-directed energy deposition of 316L and 316LSi was explored

BY D. PICCONE, L. HAGEN, S. TATE, AND J. KLEMM-TOOLE

Abstract

Gas metal arc-directed energy deposition (GMA-DED) is a high deposition rate additive manufacturing process ideal for producing large structural components. Incomplete fusion (IF) is a common defect in GMA-DED, so understanding IF formation and its impact on mechanical properties is important. This work used 316L and 316LSi feedstocks to fabricate GMA-DED builds with increasing hatch spacing to systematically induce IF. A combination of in-situ thermography and ex-situ optical microscopy was employed to determine the size and frequency of pores in the builds. With increasing hatch-spacing-to-bead-width ratio, the maximum size and frequency of IF defects increased, although smaller and fewer defects were observed in 316LSi relative to 316L. The tensile properties of 316L responded non-monotonically to increasing hatch-spacing-to-bead-width ratio, and the difference in tensile properties between samples loaded parallel to the build direction and parallel to the welding direction appeared to be more strongly influenced by crystallographic texture rather than the presence of IF defects. The 316LSi showed no statistically significant influences of hatch-spacing-to-bead-width ratio or loading direction on tensile properties, indicating that 316LSi is more robust to the evaluated process variations and should be considered for structural applications.

Keywords

- Gas Metal Arc Directed Energy Deposition
- Wire Arc Additive Manufacturing
- Wire Arc Directed Energy Deposition
- Incomplete Fusion Defects
- 316L
- 316LSi
- Tensile Testing

https://doi.org/10.29391/2025.104.023

Introduction

Gas metal arc-directed energy deposition (GMA-DED), also known as wire arc additive manufacturing or wire arc-directed energy deposition, is being considered as a potential manufacturing method to produce large structural components in power generation applications, such as piping headers or valve bodies. A key advantage of using GMA-DED for this application is the high deposition rate that can avoid long lead times associated with casting and forging while creating larger-scale parts compared to laser powder bed fusion (LPBF) (Ref. 1). However, a deeper understanding of defect formation in GMA-DED and resulting mechanical properties is needed. Defects in GMA-DED can result from multiple factors, including contamination, unstable weld processes, and poor tool-path selection (Ref. 1). Incomplete fusion (IF) defects arise from a failure of the weld bead to fuse to the base material, previous layers, or adjacent weld beads. Issues with weld bead fusion can result from insufficient heat input, incorrect tool path, or travel speed that is too great (Ref. 2). In LPBF, IF defects originate from insufficient overlap between neighboring melt pools (Ref. 3). Similarly, IF defects in GMA-DED occur between neighboring weld beads due to too-large hatch spacing or too-low heat input, leading to insufficient melt pool overlap (Refs. 4, 5).

Investigations of the influence of IF on the tensile properties of LBPF 316L have found that these defects are a source of anisotropic elongation. Still, they have a limited effect on yield strength (Ref. 6). The formation of IF in LPBF was found to be elongated parallel to the heat source travel

Table 1 — Typical Wire Composition (wt-%) of Lincoln Electric Blue Max® 316L (Ref. 10) and Lincoln Electric Red Max® 316LSi Reported by the Wire Feedstock Manufacturer (Ref. 11) and Compositions of Builds Made From the Feedstocks

	%C	%Cr	%Cu	%Mn	%Mo	%N	%Nb	%Ni	%P	%S	%Si
Lincoln Electric Blue Max® 316L	0.01–0.02	18.5–18.7	0.03–0.13	1.6–1.8	2.1–2.6	0.03	0.01 max.	11.8–12.2	0.02	0.01 max.	0.39–0.40
Lincoln Electric Red Max® 316LSi	0.01–0.02	18.2–18.3	0.07–0.10	1.7	2.3	0.06 – 0.07	0.01 max.	11.3	0.02	0.02	0.79–0.87
GMA-DED 316L	0.02	18.26	0.39	1.62	2.20	0.01	0.01	11.83	0.023	0.019	0.36
GMA-DED 316LSi	0.02	18.47	0.23	1.69	2.47	0.06	0.01	11.41	0.02	0.016	0.81

direction. High stress concentrations arose from loading an elongated pore perpendicular to the major axis; thus, loading along the build direction introduced the highest stress concentrations (Ref. 6). Crystal plasticity modelling of LPBF 316L further supported the role of high aspect ratio IF on anisotropic elongation, where vertically loaded samples displayed lower elongation compared to horizontal samples (Ref. 7). In extreme cases, it was found that intentionally introduced pores began to impact ultimate tensile strength and total elongation only when pore diameter reached 16% and 9% of the cross-sectional area, respectively (Ref. 8).

In GMA-DED, IF typically displays elongated geometries. However, the influence of asymmetrical IF defects on tensile properties in GMA-DED has been studied less (Ref. 5). Some work has been performed to study the impact of gas pores on GTA-DED Ti-6Al-4V. The use of contaminated wire feedstock-induced pores of approximately 100 µm in diameter resulted in a reduction in density from 99.9% in the control build to 99.6% in the contaminated build. It was shown that both builds had comparable yield strength and tensile strength but that the contaminated samples displayed lower elongation (Ref. 9).

While some work has been done to study the impacts of small gas pores, limited work has been done to study IF defects within GMA-DED and their impact on mechanical properties. This study evaluates the impact of systematically introduced IF defects on tensile properties on GMA-DED of the commonly used austenitic stainless steel feedstocks 316L and 316LSi. The results of this work are expected to provide insight into the impact of process-induced IF defects on mechanical properties and build confidence in using GMA-DED to produce large components for structural applications.

Experimental Methods

Build Parameters and Wire Compositions

A Universal Robots UR10e collaborative robot with a Fronius TPS400i gas metal arc welding power source was used to make GMA-DED builds. The high heat input pulse multi control transfer mode with an average current of 210 A and potential of 22 V was used with 1.14 mm (0.045 in.) diameter Lincoln Electric Blue Max® 316L and Red Max® 316LSi wire feedstocks at a wire feed speed of 1.02 mm/min (400 in./min) and a heat source travel speed of 17 mm/s (40 in./min), resulting in a deposition rate of approximately 5 kg/h. A shielding gas of 95% Ar and 5% CO_2 with a gas flow rate of 11.8 liters/min (25 ft^3/h) was used during deposition. A pause time of 30 s was used between passes. Compositional ranges provided by the feedstock supplier of the 316LSi and 316L wire feedstock are shown in Table 1, where wt-% ranges are reported for major alloying elements and max wt-% is reported for trace elements. GMA-DED build chemistries were tested with optical emission spectroscopy, and values are reported in Table 1. Builds measuring approximately 127 mm × 102 mm × 51 mm (5 in. × 4 in. × 2 in.) were constructed using a parallel bead tool path, shown in Fig. 1. After construction, all builds were heat-treated at 1040°C for one hour and water quenched.

The hatch spacing was selected by performing single-layer builds with varying spacing using the weld parameters outlined above. The hatch spacing that resulted in a defect-free single-layer build was selected as the baseline, and then bead spacing was increased by 0.5 mm and 1 mm from this baseline. This process was done for both the 316L and 316LSi wire fillers. Additionally, bead width was measured for both materials to calculate the hatch-spacing-to-bead width ratio.

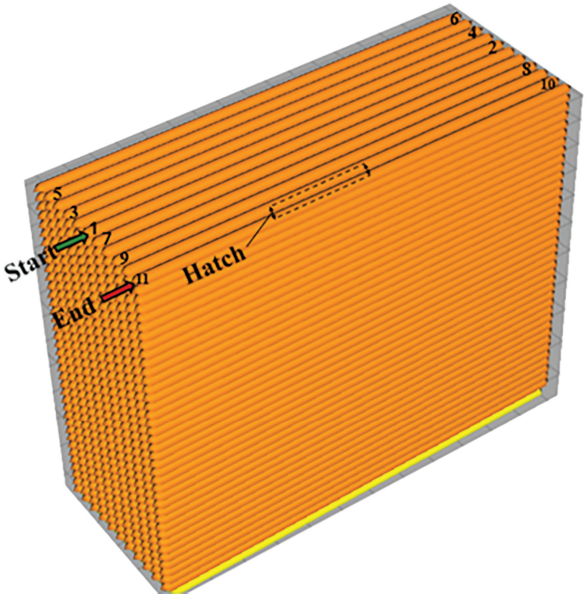

Fig. 1 — Schematic figure of build geometry and weld pathing used for 316L and 316LSi builds, including hatch spacing and travel directions where the numbers correspond to the deposition order.

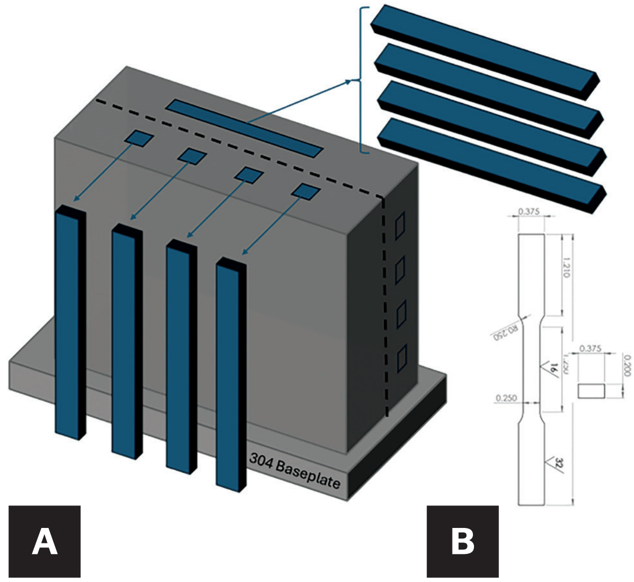

Fig. 2 — A — Schematic of builds used for the incomplete fusion defect study showing tensile bar layout; B — drawing of the tensile specimen machined from the builds. Dimensions are in inches.

Table 2 — Parameters Used to Make Builds with Systematically Introduced IF

Build	Feedstock	Bead Width (mm)	Hatch Spacing (mm)	Hatch-Spacing-to-Bead-Width Ratio
1	316L	5.1	3.0	0.58
2	316L	5.1	3.5	0.68
3	316L	5.1	4.0	0.78
4	316LSi	5.6	3.5	0.63
5	316LSi	5.6	4.0	0.71
6	316LSi	5.6	4.5	0.80

The hatch spacing, bead width, and hatch-spacing-to-bead-width ratio are summarized in Table 2.

It should be noted that the hatch spacings employed for 316L and 316LSi were different. Higher silicon content reduces the surface tension of the melt pool, leading to greater fluidity and wider melt pools in 316LSi (Ref. 2). The wider beads in 316LSi required larger hatch spacings to maintain similar hatch-spacing-to-bead-width ratios with 316L. It should be noted that the calculated hatch-spacing-to-bead-width ratios are determined only by the specific welding parameters, shielding gas, and composition of the specific alloy. Any changes in filler composition, shielding gas, or welding parameters will change the hatch-spacing-to-bead-width ratios.

IF Detection and Characterization

A Xiris XIR-1800 short-wavelength infrared thermal camera was used to monitor the incomplete fusion during deposition. Video capture was performed at 1000 frames per second from a side view with a focal distance of 400 mm. Video was captured to record 22 deposition passes over two layers.

MagnaFlux dye penetrant was used to identify IF in builds. Builds were sectioned to expose the face perpendicular to the transverse direction, and approximately 26 cm^2 (4 $in.^2$) of cross-sectional face was sampled for each build condition. Samples were cleaned and penetrants were applied then thoroughly cleaned and developed to locate IF defects. Areas

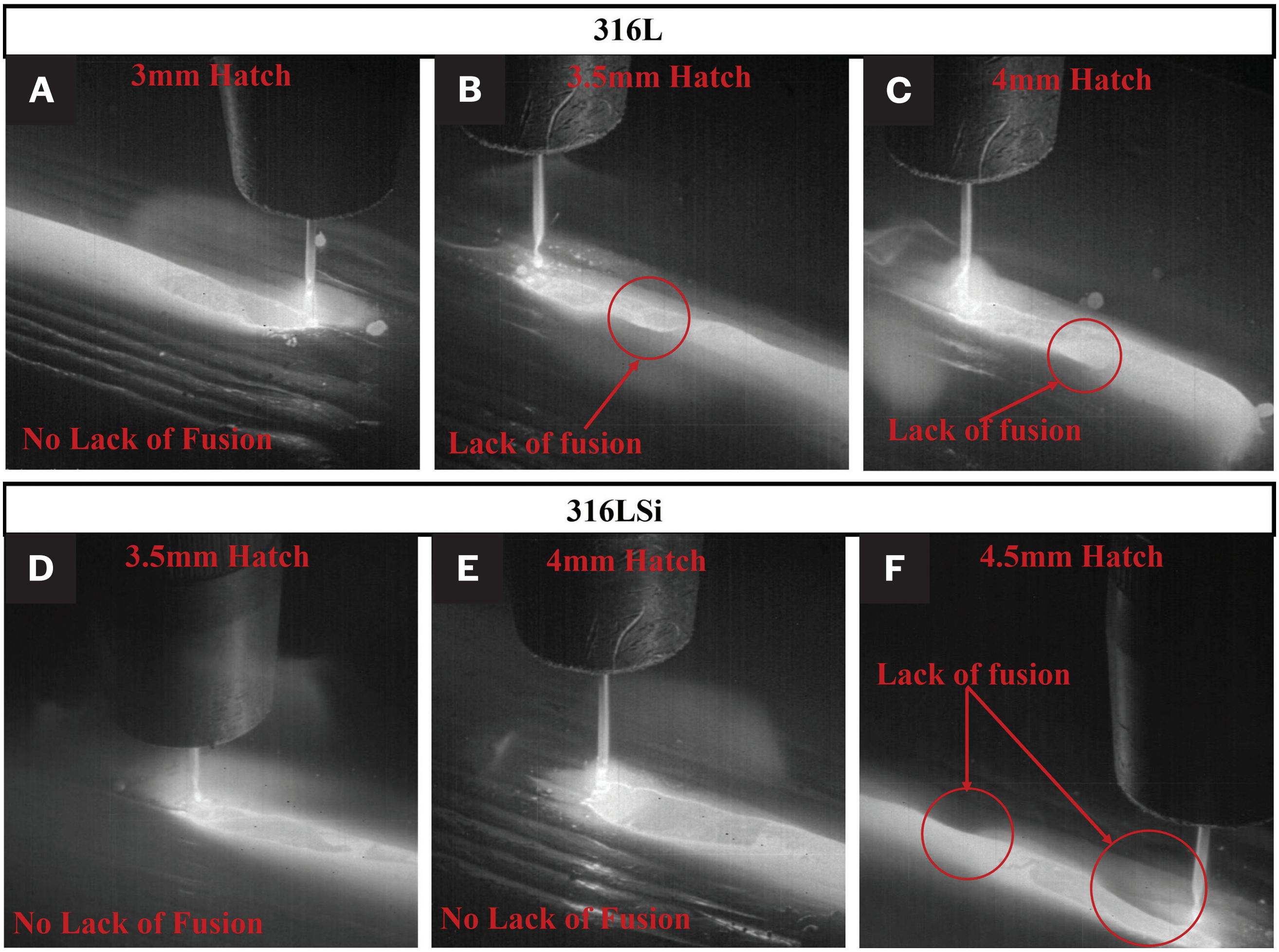

Fig. 3 — In-situ thermography during deposition of 316L with: A — 3 mm; B — 3.5 mm; C — 4 mm hatch spacings. 316LSi with: D — 3.5 mm; E — 4 mm; F — 4.5 mm hatch spacings. When observed, IF defects are noted.

where IF was detected with dye penetrant were then metallographically prepared and imaged with optical microscopy.

Microstructure Characterization and Fractography

Metallographic specimens were taken transversely to the travel direction in each build condition and polished down to 1 µm diamond suspension. Electron backscatter diffraction (EBSD) samples were further vibratory polished with 0.05 µm colloidal silica for 12–24 h. EBSD was performed with an FEI Helios Nanolab scanning electron microscope (SEM) with an accelerating voltage of 20 kV and a step size of 1.5 µm for low magnification scans and 0.4 µm for high mag postmortem scans. Optical micrographs were taken with a DSX 500.

To analyze fracture surfaces, macro and SEM fractography were performed. Macro fractographs were captured with a Nikon DSLR camera equipped with a macro lens. SEM fractography was performed in secondary electron mode with an FEI Helios Nanolab FIB-SEM and an accelerating voltage of 10 kV.

Tensile Testing

To investigate the influence of defects on tensile behavior, eight rectangular dog bone tensile bars, four parallel (vertical) to the build direction and four perpendicular to the build direction (horizontal) were machined from each build condition to the geometry shown in Fig. 2. Tensile tests were performed on the MTS 6 Landmark 22.5 kip servo-hydraulic load frame with a 25 mm (0.984 in.) extensometer at an engineering strain rate of $1 \times 10^{-3} s^{-1}$ in accordance with ASTM E8, *Standard Test Methods for Tension Testing of Metallic Materials* (Ref. 12). Samples were gripped with hydraulic wedge grips, and force-displacement data was collected via MTS software and further processed to extract yield strength, tensile strength, uniform elongation, and post-uniform elongation for each sample.

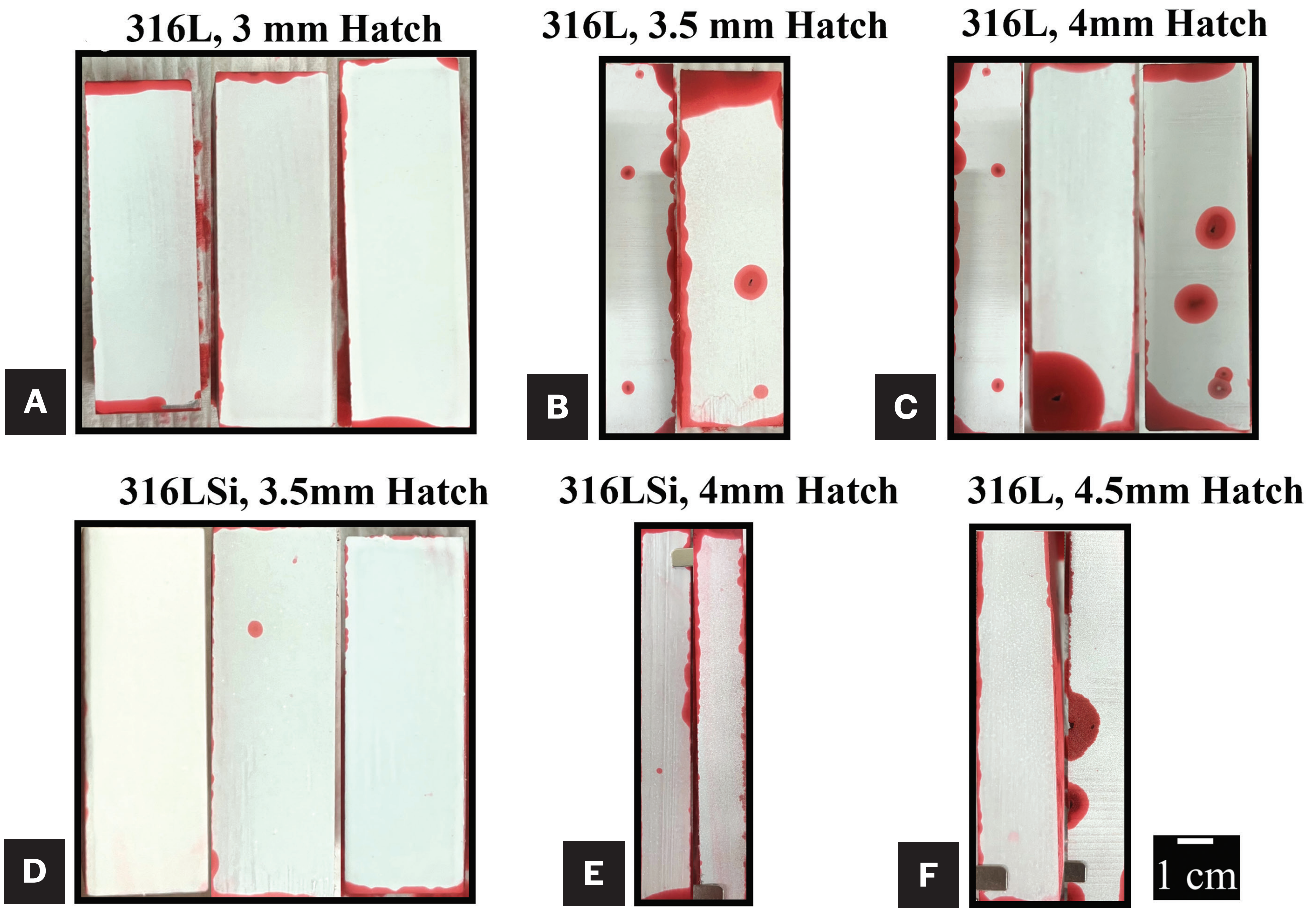

Fig. 4 — Dye penetrant results from 316L with: A — 3 mm; B — 3.5 mm; C — 4 mm hatch spacings. 316LSi with: D — 3.5 mm; E — 4 mm; F — 4.5 mm hatch spacings. Sections totaling 26 mm² were inspected for each condition.

Results

Incomplete Fusion Detection and Characterization

The builds were monitored with in-situ thermography to observe IF defect formation. The results, shown in Fig. 3, indicated IF was observed more frequently with increasing hatch spacing in 316L and 316LSi. No incomplete fusion was observed at the lowest hatch spacing for 316L (3 mm) and 316LSi (3.5 mm), but it was observed for the larger hatch spacings of 3.5 and 4 mm in 316L. Conversely, incomplete fusion was only observed at the highest hatch spacing of 4.5 mm in 316LSi, indicating that 316LSi is less susceptible to IF formation. Figure 5F shows a pass being deposited on a previously formed IF defect. However, the thermography did not indicate if this IF defect was filled with subsequent layers. The IF defects could be seen to form at the edge of the deposition passes in each case, and they were elongated parallel to the travel direction.

Initially, sections of the builds were taken and metallographically mounted to characterize IF defects. No defects were found when metallographic sections were taken at consistent locations within the builds. To better detect pores that remained after the build process, dye penetrant inspection was performed on large cross sections, as shown in Fig. 4. Despite the consistent observation of IF defects between deposition passes observed with in-situ thermography, IF defects were randomly distributed in the final builds. Samples were taken where dye penetrant indicated IF defects for further characterization.

Once IF defects were identified using dye penetrant, samples were metallographically prepared, and their morphology was characterized using light optical microscopy (LOM). Figure 5 shows that IF defects had high aspect ratios and a major axis length on the millimeter scale. Samples were sectioned perpendicular to the travel direction of the deposition passes. Thus, the IF defects were likely elongated out of the plane of the images, as indicated by the morphology observed during thermography. Figure 5D displays a pore in the lowest hatch spacing condition of 316LSi, although no IF was observed in thermography. It is possible that due to the more spherical shape, the pore in Fig. 5D is a gas pore (Ref. 2).

IF defect sizes were measured from micrographs in Fig. 5 and defect frequency (number of defects per area) was

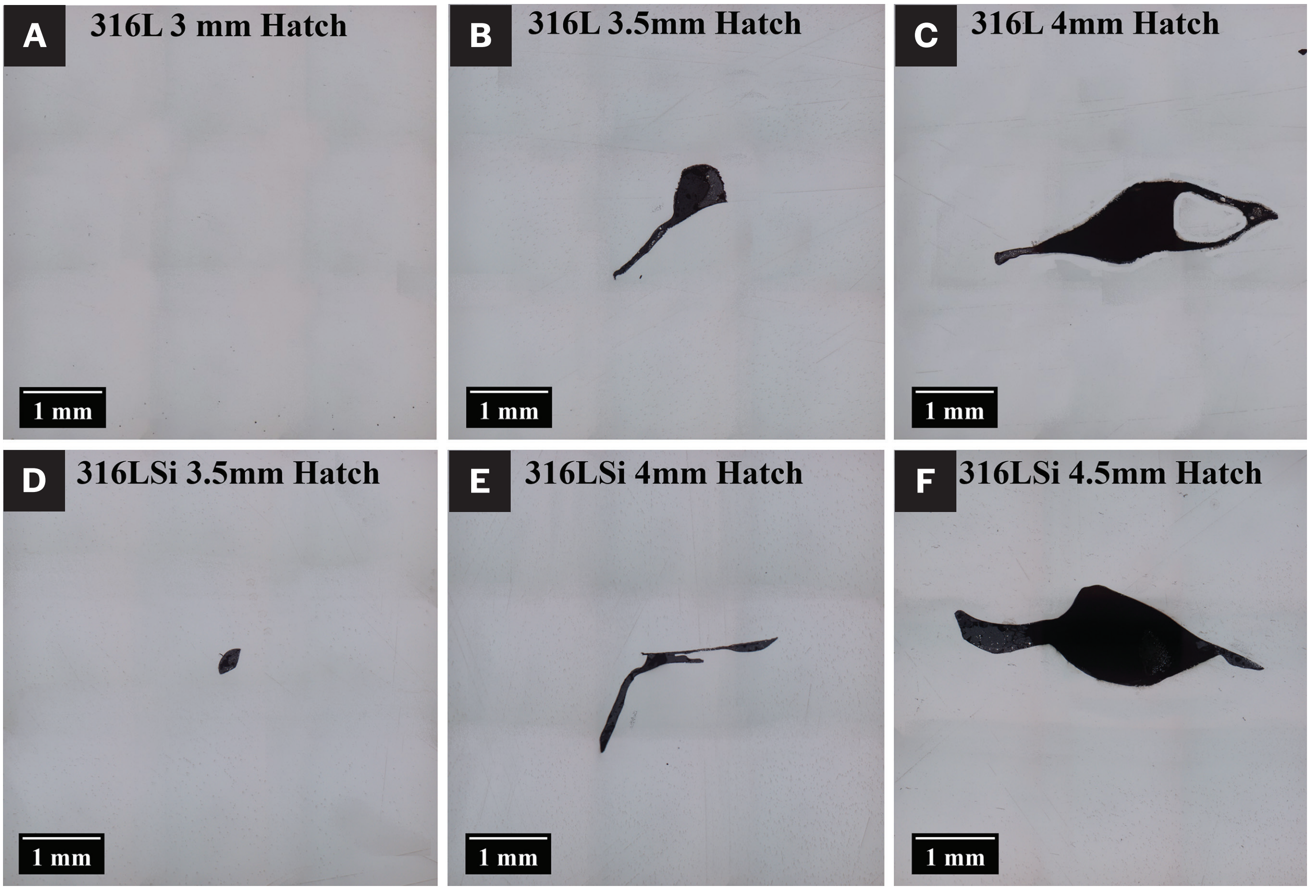

Fig. 5 — Optical micrographs of IF defects in 316L with: A — 3 mm; B — 3.5 mm; C — 4 mm hatch spacings. 316LSi with: D — 3.5 mm; E — 4 mm; F — 4.5 mm hatch spacings, indicating an increase in IF defect size as hatch spacing increased.

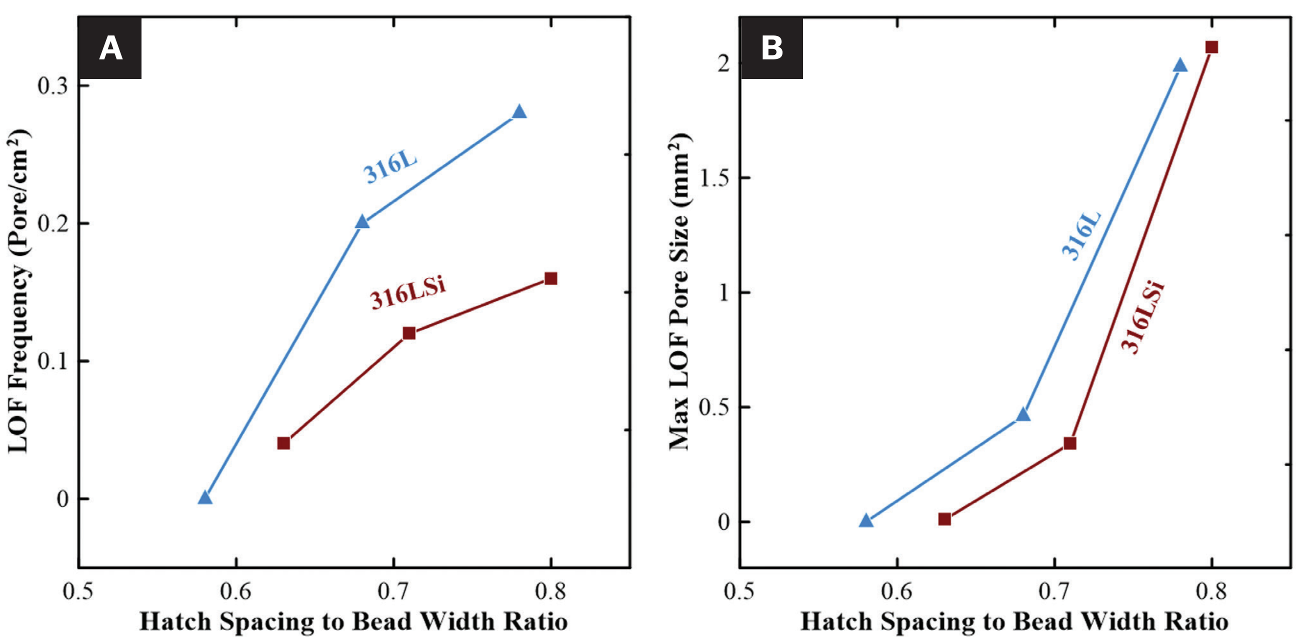

Fig. 6 — A — IF defect frequency; B — IF max defect size as a function of hatch-spacing-to-bead-width ratio for 316L and 316LSi.

measured from large sections inspected via dye penetrant analysis in Fig. 4. The variations of IF defect frequency and size based on hatch-spacing-to-bead-width ratio for 316L and 316LSi are shown in Fig. 6. The frequency (Fig. 6A) and maximum defect size (Fig. 6B) both increased with increasing hatch-spacing-to-bead-width ratio for 316L and 316LSi. However, in general, 316LSi showed smaller and less frequent IF defects for a given hatch-spacing-to-bead-width ratio, again indicating that 316LSi was less susceptible to IF defect formation.

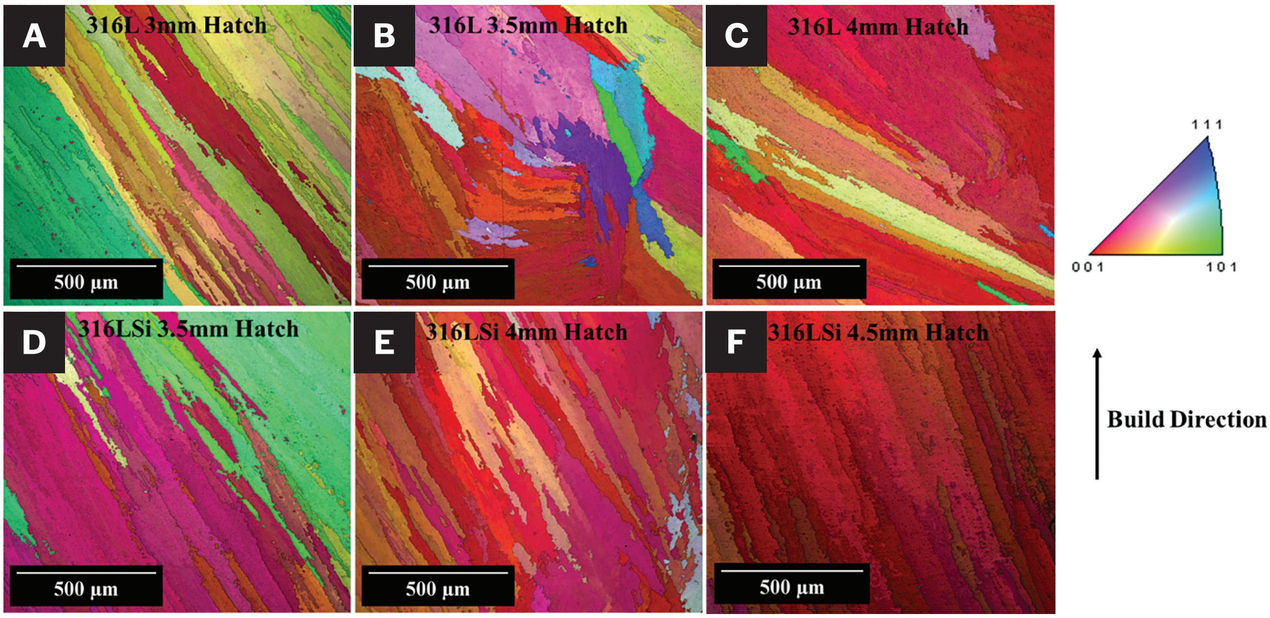

Fig. 7 — EBSD IPF + IQ maps of 316L with: A — 3 mm; B — 3.5 mm; C — 4 mm hatch spacing. 316LSi with: D — 3.5 mm; E — 4 mm; F — 4.5 mm hatch spacings. Images were taken from sections perpendicular to the direction of the deposition pass travel. The build direction is vertical in all of the images, and the coloration of the IPF maps is relative to the build direction.

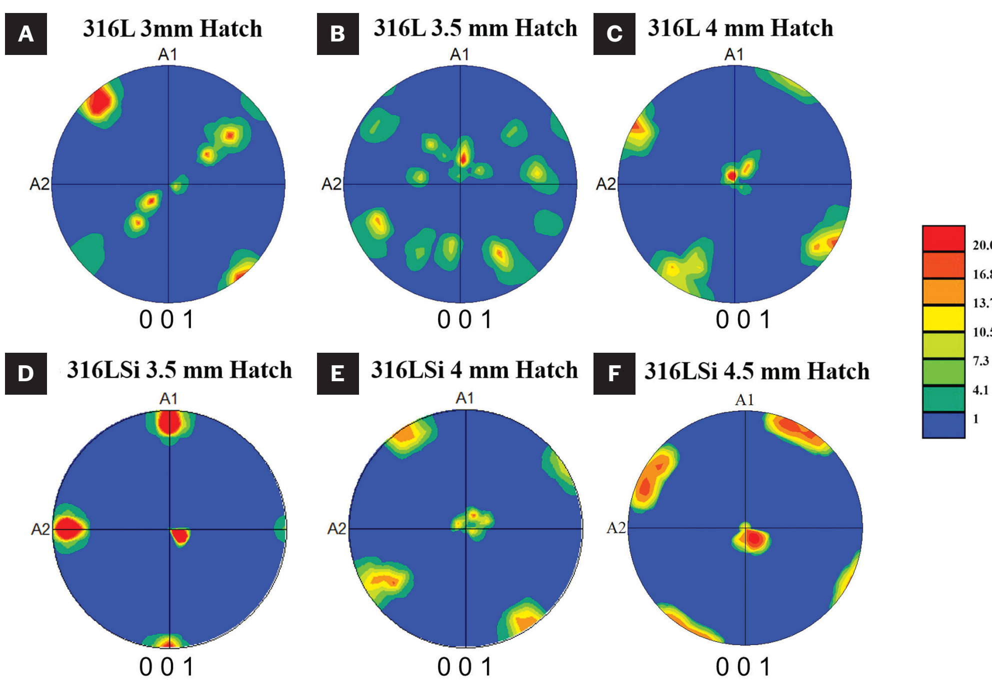

Fig. 8 — (001) pole figures of 316L with: A — 3 mm; B — 3.5 mm; C — 4 mm hatch spacings. 316LSi with: D — 3.5 mm; E — 4 mm; F — 4.5 mm hatch spacings. The pole figures correspond to the EBSD IPF + IQ maps from Fig. 7. The center of the pole figures corresponds to the build direction.

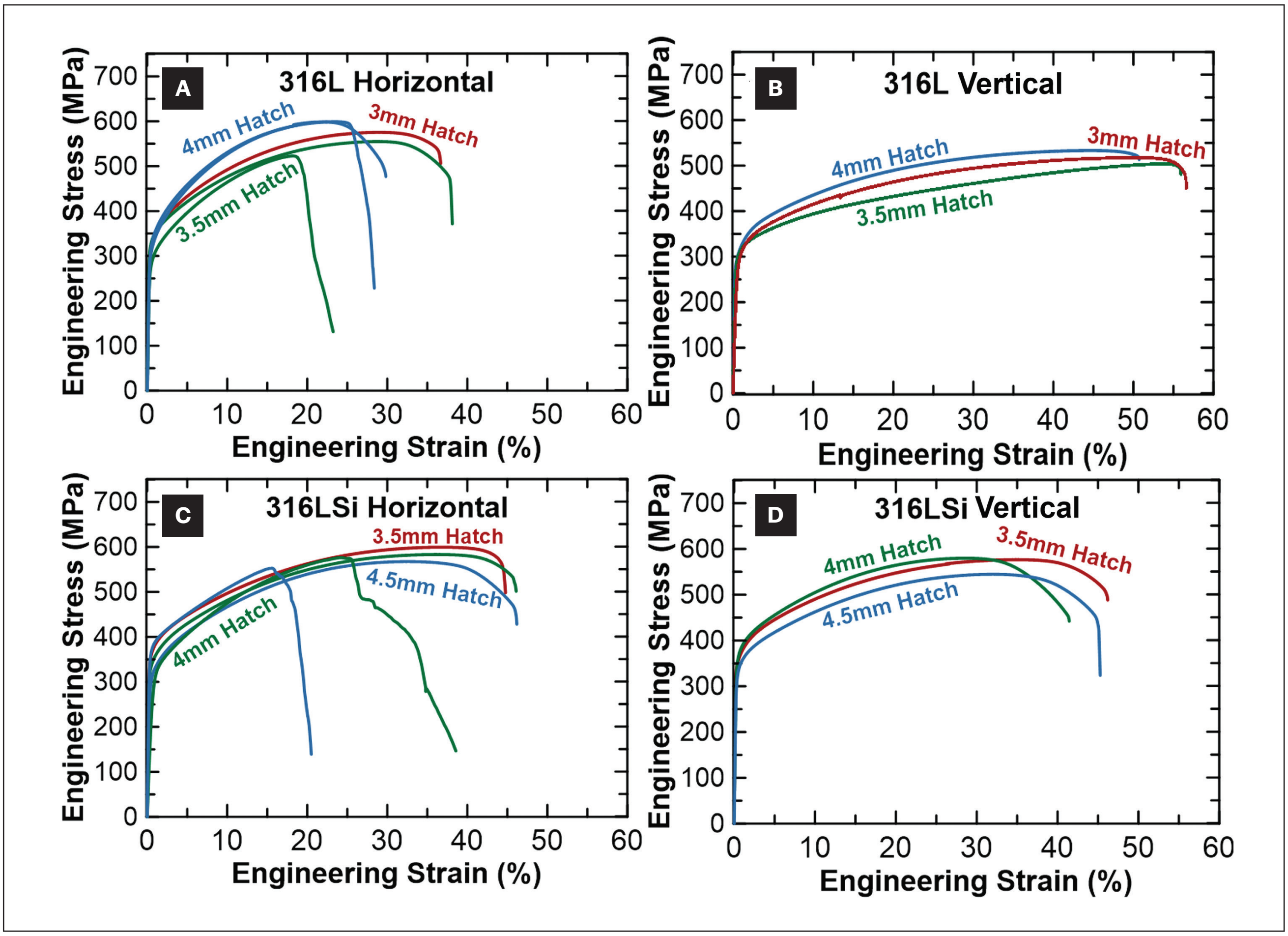

Fig. 9 — Representative engineering stress-strain curves of: A — 316L horizontal; B — 316L vertical; C — 316LSi horizontal; D — 316LSi vertical samples. Curves indicating IF-driven premature failure are shown as well.

Grain Morphology and Crystallographic Texture

Superimposed inverse pole figure (IPF) and image quality maps obtained with EBSD from representative sections of the build are shown in Fig. 7. In general, all of the conditions showed columnar grains elongated approximately parallel to the build direction, which is typical of directed energy deposition processes of austenitic stainless steels (Refs. 13, 14). Some grains appeared elongated at an angle relative to the build direction. However, this was likely due to the location of the scan relative to the melt pool boundary. Average grain width was nominally consistent across conditions, but the grain lengths are larger than the field of view of the scans. Figure 8 shows pole figures generated from the IPF maps in Fig. 7. Generally, (001) planes were roughly parallel to the build direction, although some additional texture components were likely present.

Influence of Hatch Spacing and IF Defects on Mechanical Properties

Figure 9 shows representative engineering stress-strain curves for each condition and samples that showed distinctly low tensile elongation, indicating defect-driven failure. Premature failure was primarily observed only in horizontal 316L and 316LSi samples, with increasing frequency as the hatch spacing increased. Close inspection of Figs. 9A and C indicated that samples that exhibited premature failure, likely due to IF defects, generally displayed a similar yielding and early strain hardening response to samples without premature failure, indicating the IF defects only influenced later stages of deformation and initiation of fracture. There was a significant anisotropy observed from stress-strain curves of 316L, where horizontal samples showed greater strain hardening and lower elongation than vertical ones. In contrast, 316LSi horizontal and vertical samples showed more-similar stress-strain curves that were more comparable to horizontal 316L samples.

Figure 10 shows a summary of strength properties as a function of hatch spacing and loading direction from the tensile testing results of 316L and 316LSi. Figure 10A shows the influence of loading orientation on the elastic modulus

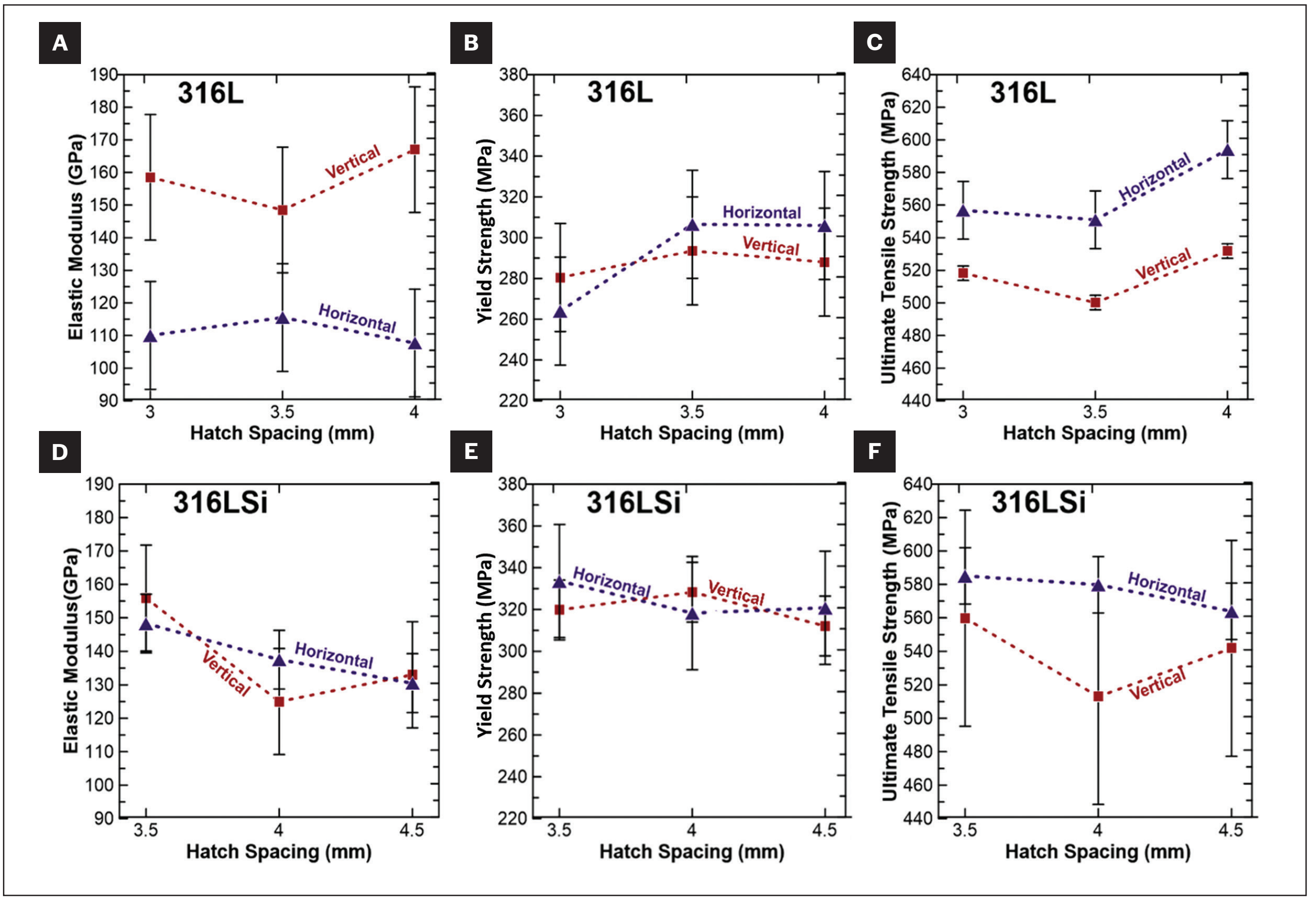

Fig. 10 — Influences of hatch spacing on 316L: A — Elastic modulus; B — yield strength; C — ultimate tensile strength, and 316LSi; D — elastic modulus; E — yield strength; F — ultimate tensile strength. In each plot, symbols are mean values and bars are 95% confidence intervals based on pooled standard deviations. Means were calculated from four measurements.

(taken to be the slope of the elastic portion of the stress-strain curves) in 316L, where vertical samples exhibited higher moduli compared to horizontal samples. The difference in elastic properties based on loading direction was likely a result of the observed texture; similar observations have been made throughout a wide range of wire DED processes for austenitic stainless steels (Ref. 15). Increases in IF defects induced by increasing hatch spacing did not show a statistically significant effect on yield strength of 316L, as shown in Fig. 10B, which was also seen in the stress-strain curves in Fig. 9. However, increases in hatch spacing and the occurrence of IF did significantly influence the ultimate tensile strength, although higher values were observed for larger hatch spacings, which is not what would be expected. Across all hatch spacings, horizontal 316L samples showed higher UTS values compared to vertical ones. Unlike 316L, no statistically significant influences of hatch spacing or loading orientation were observed with 316LSi.

Figure 11 shows a summary of ductility properties as a function of hatch spacing and loading direction from the tensile results of 316L and 316LSi. Figure 11A shows that there was a non-monotonic change in uniform elongation with increasing hatch spacing for 316L as well as an overall higher uniform elongation of vertical samples compared to horizontal ones. Figure 11B shows that post-uniform elongation did not show statistically significant change with hatch spacing, which was somewhat unexpected, as it would be anticipated that the increased occurrence of IF defects would decrease this value. Figure 11C indicates the same trend of total elongation with hatch spacing as shown in Fig. 11A for uniform elongation. The variation in total elongation in 316L shown in Fig. 11C was most likely a manifestation of variations in uniform elongation because post-uniform elongation did not show significant variation with hatch spacing, as shown in Fig. 11B. In contrast, 316LSi showed no significant influence of hatch spacing or loading direction on ductility properties. Overall, Figs. 10 and 11 show that the tensile properties of 316LSi are far less sensitive to variations in hatch spacing and loading orientation compared to 316L.

Fracture Behavior

In general, all of the fracture surfaces displayed predominantly microvoid coalescence regardless of whether LOF defects were present. Figure 12A shows the fracture surface of a horizontally loaded 316L sample with a 4 mm hatch that displayed premature failure, resulting in total

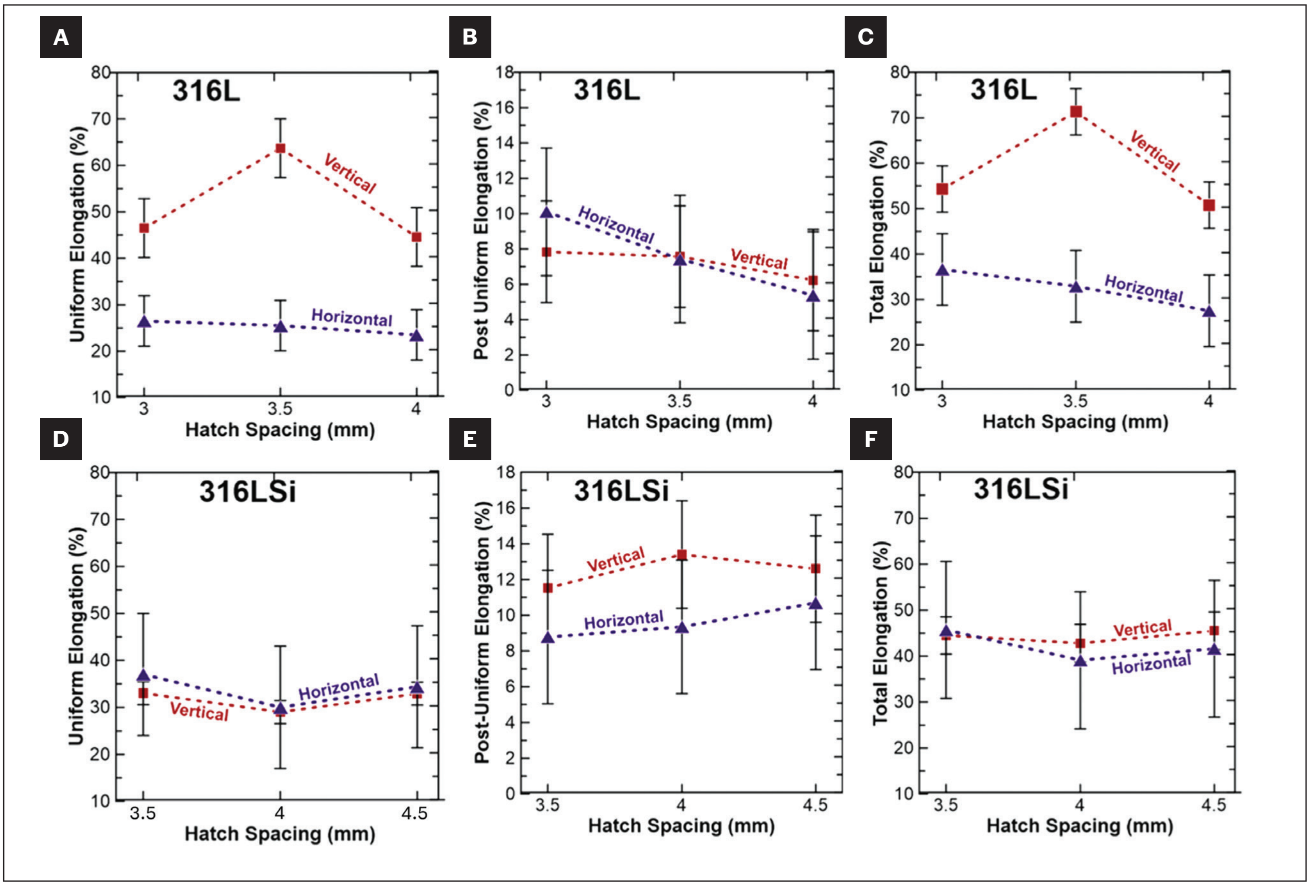

Fig. 11 — Influences of hatch spacing on 316L: A — Uniform elongation; B — post uniform elongation; C — total elongation, and 316LSi; D — uniform elongation; E — post uniform elongation; F — total elongation. In each plot, symbols are mean values and bars are 95% confidence intervals based on pooled standard deviations. Means were calculated from four measurements.

elongation of 12.9% with an IF defect on the fracture surface. Figure 12B shows a vertical 316L sample with a 3.5 mm hatch with a similar size IF defect that did not show premature failure, resulting in a total elongation of 72.9%. In both cases shown in Fig. 12, IF defects on fracture surfaces were observed to compose approximately 2.3% of the total cross-sectional area, although vastly different total elongations were observed. It appears that the influence of IF defects on ductility is more complex than would be assumed with the theory that bigger and more frequent defects lead to lower elongation.

Discussion

Development of IF defects

The difference in frequency of IF pore formation between deposition passes imaged with in-situ thermography and the low occurrence of defects observed in the builds suggests that the process of defect retention after several deposition passes was highly stochastic. Furthermore, the infrequent observation of IF defects retained in the build likely indicates that IF defects can be remelted or filled with subsequent passes. When IF forms between two neighboring deposition passes due to a sufficiently large hatch-spacing-to-bead-width ratio, the IF defect is a surface defect, as shown in Fig. 13A. Whether the surface defect is retained in the build as a pore depends on the conditions of the deposition passes in the next layer. Figure 13B suggests that if the next deposition pass remelts or fills liquid into the previously formed incipient IF, no pore will be retained in the build. However, if the subsequent insufficiently remelts the incipient IF, the pore will remain. It appears that it is highly stochastic whether a pore will be remelted with subsequent passes, but remelting seems to occur more frequently with 316LSi, likely due to the well-known higher fluidity characteristic of the higher Si content. It is therefore likely that 316LSi forms smaller and less frequent IF pores for a given hatch-spacing-to- bead-width ratio due to the greater ability to fill incipient surface IF pores from previous layers.

Influence of Texture and Composition on Deformation Behavior

A significant number of austenite grains had (001) directions parallel to the build direction in the GMA-DED builds, which has been observed by others as well (Refs. 13, 14). However, the (001) texture in this work was not as strong

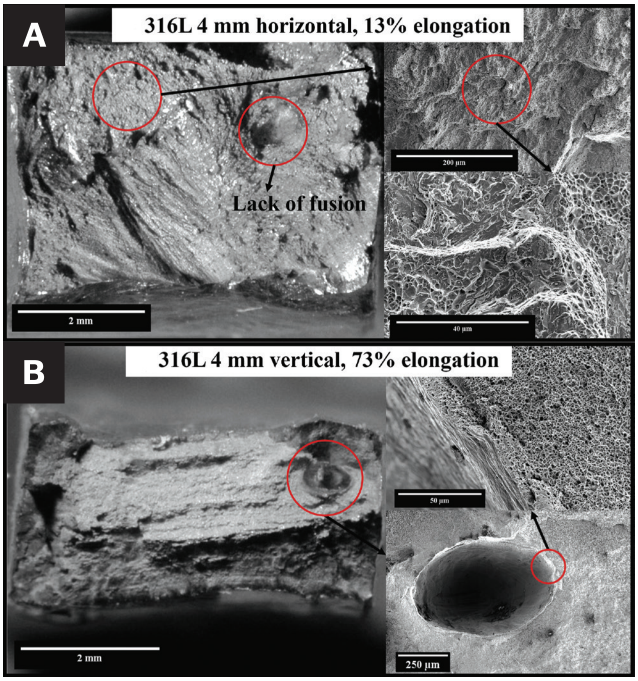

Fig. 12 — SEM SE micrographs of fractures from: A — Horizontal 316L 4 mm hatch with 12.9% ; B — 316L 4 mm hatch with 72.5% elongation, both displaying ductile fracture in the presence of IF defects.

it was in previous studies, likely due to the builds being multipass. It has been observed elsewhere that multipass builds show a weaker (001) parallel to the build direction texture than single-pass wide builds produced with laser wire directed energy deposition (Refs. 14, 16). Despite the somewhat weaker texture observed in the GMA-DED builds in this work, the texture that was present did lead to differences in the dominant crystallographic direction that was parallel to the loading axis in vertical and horizontal samples. Figure 14 shows (001), (101), and (111) pole figures of a 316LSi sample with a 3.5 mm hatch, where the center of the pole figure is the tensile loading direction. In horizontal samples, the tensile axis was parallel to the [101] direction, while the tensile axis was primarily parallel to the [001] direction in vertical ones.

It has been observed that differences in textural components relative to loading orientation can affect deformation mechanisms in additively manufactured 316L. Wang et al. investigated crystallographic orientation dependence of tensile properties in LBPF 316L, where samples loaded parallel to [101] and [111] directions showed more twinning than those loaded parallel to [001] directions (Ref. 17). In this work, greater amounts of strain hardening were observed in horizontal components where the tensile axis was parallel to [101] directions compared to vertical ones where the tensile axis was parallel to [001] directions. The results from Wang et al. would indicate that perhaps the greater amount of strain hardening is potentially due to a change

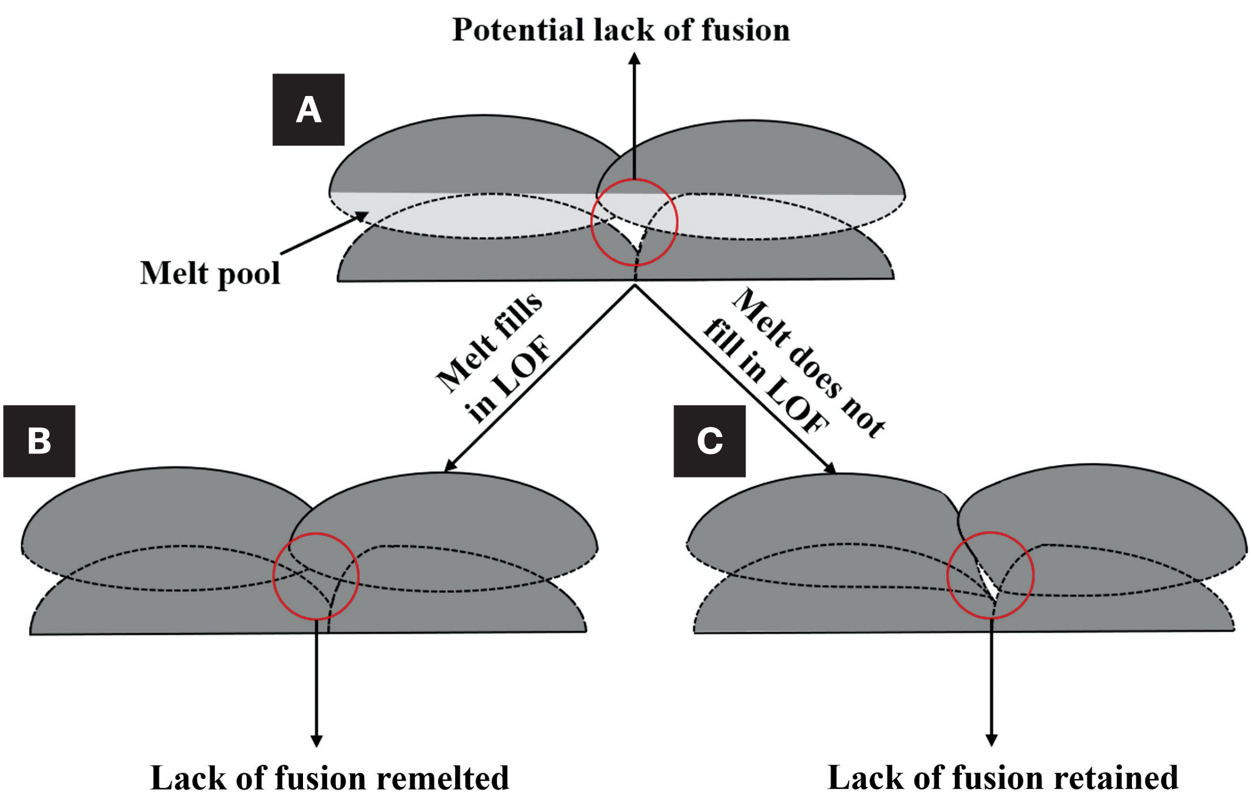

Fig. 13 — Schematic of the process of remelting IF defects.

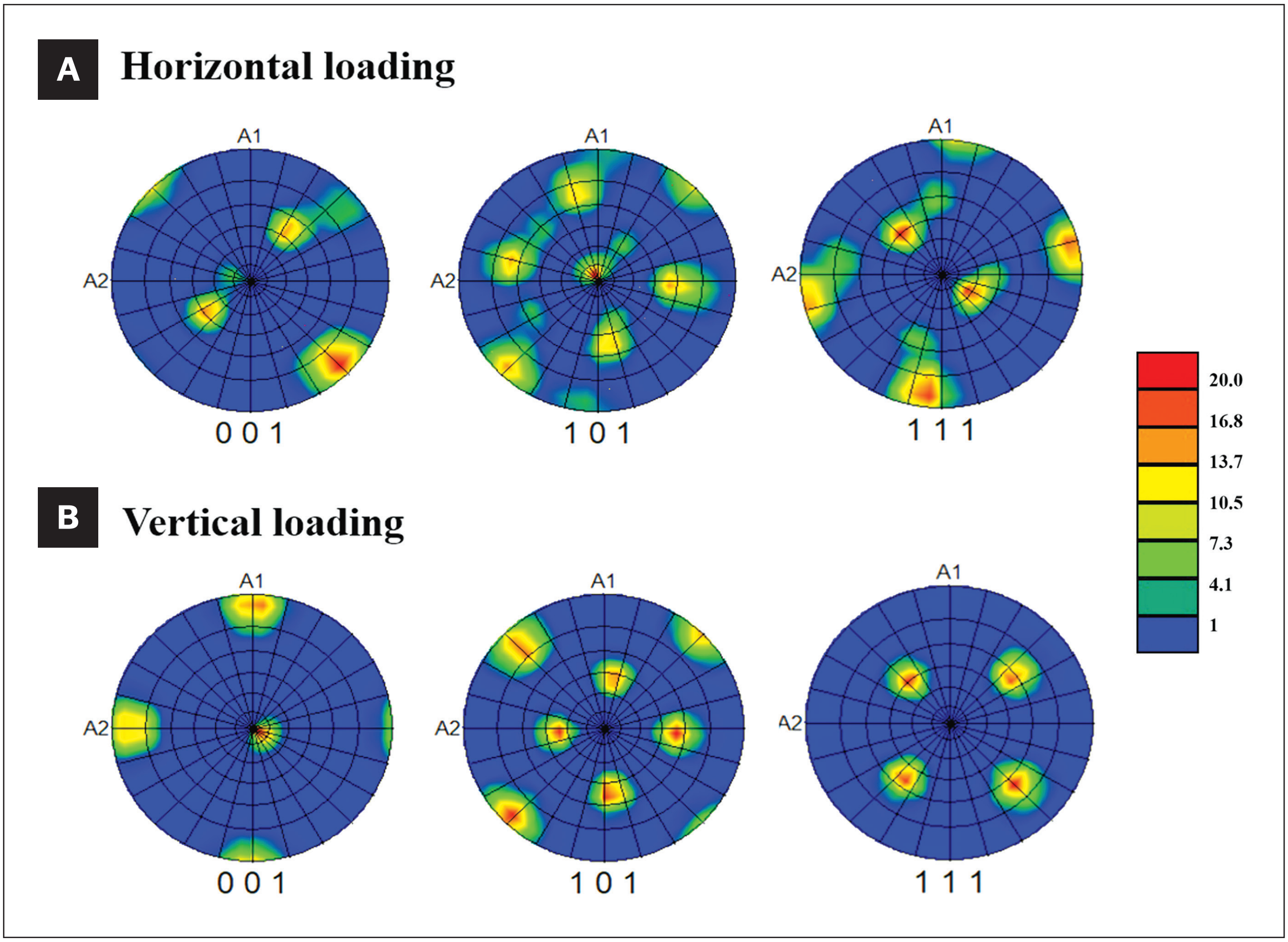

Fig. 14 — (001), (101), and (111) pole figures of 316LSi with a 3.5 mm hatch showing which crystallographic directions are parallel to the tensile loading axis (center of pole figures) for: A — Horizontally loaded samples; B — vertically loaded samples.

in deformation mechanism with an increase in twinning. Composition also influences the tendency to twin during deformation via changes in stacking fault energy. It has been shown that increases in Si and reductions in Ni in 316L, which represent the major differences between 316LSi and 316L, lower the stacking fault energy, thus promoting planar slip and possibly activating other deformation mechanisms, like twinning (Refs. 18, 19). Certainly, the tensile behavior of GMA-DED of 316LSi shown in prior work has indicated the increased presence of more planar slip or even twinning compared to 316L due to higher sustained strain hardening rates during tensile deformation (Refs. 13, 19).

To determine whether changes in twinning behavior can explain some of the differences in deformation behavior observed in this work, failed tensile samples were metallographically prepared and evaluated with EBSD. In comparing horizontal and vertical 316L samples, Figs. 15A and B, respectively, it can be seen that there was a greater number of deformation twins in the horizontal sample. The difference in twinning between horizontal and vertical samples as likely due to the tensile axis being predominantly parallel to [101] directions in the horizontal samples. The effect of differences in stacking fault energy can be seen by comparing 316L and 316LSi, where the 316LSi samples in both loading orientations showed a greater amount of twinning. Generally, there was a greater difference in the amount of twinning between horizontal and vertical samples in 316L compared to 316LSi, which may explain why there was a greater difference in the strain hardening behavior based on loading direction in 316L. With the overall lower stacking fault energy in 316LSi, it was likely that differences in loading direction had a smaller effect on the initiation of twinning.

It should be noted that considerable amounts of remnant delta ferrite were observed in all of the microstructures in Fig. 15. A study of annealing behavior and deformation mechanisms in GMA-DED of 316L by Schreiber et al. found that a 1200°C solution annealing treatment dissolves delta ferrite and significantly homogenizes the microsegregation from solidification leading to an overall reduction in stacking fault energy and an increase in the amount of deformation twinning compared to the as-built condition (Ref. 21). It is possible that if more complete dissolution of the delta occurred in the samples from this work, a greater amount of twinning deformation may have occurred.

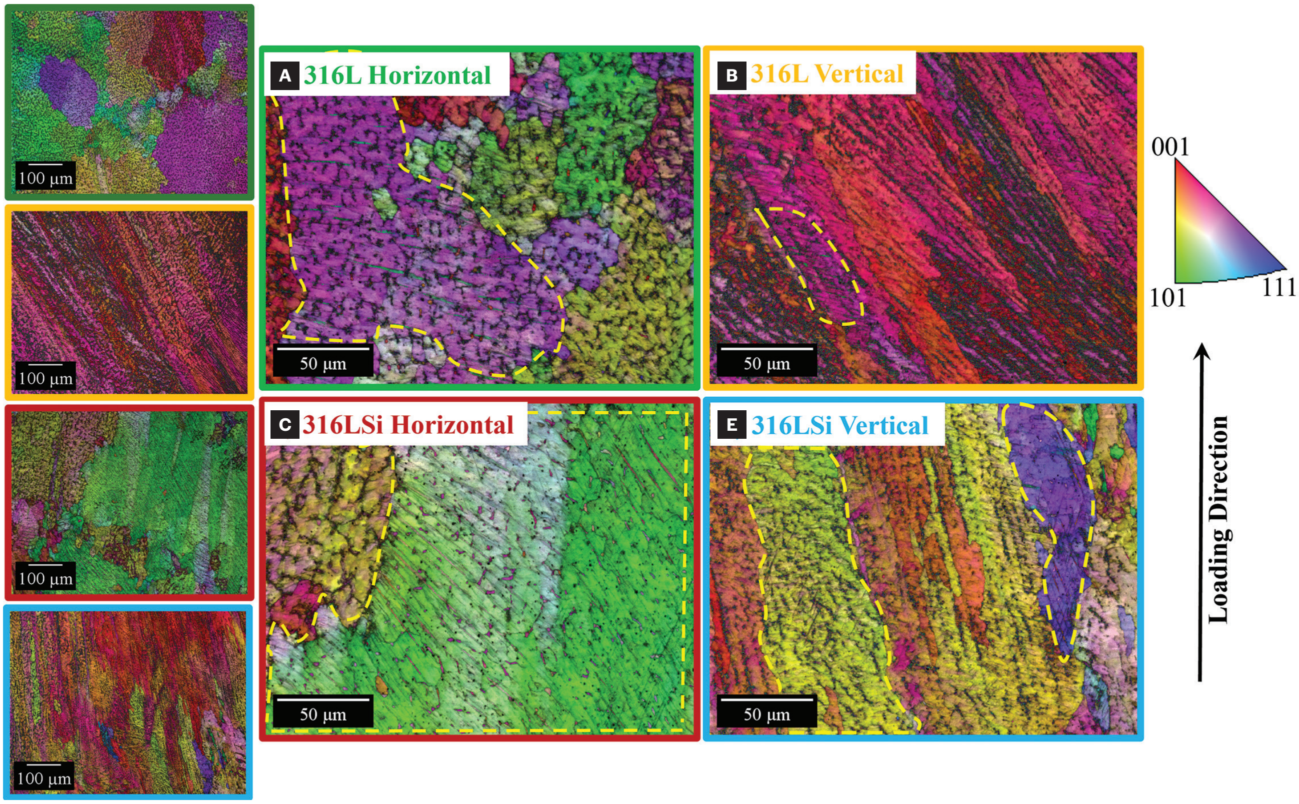

Fig. 15 — Postmortem IPF and image quality map aligned to the loading direction showing deformation twins in 316L and 316LSi with build orientation axis. Higher magnification images correspond to the respective border color and dashed lines indicate where twins were observed.

Implications for Industrial Adoption of GMA-DED of 316L/LSi

This investigation has shown that with increasing hatch spacing relative to the width of deposition passes, the size and frequency of incomplete fusion defects in the builds increased. However, for a given hatch-spacing-to-bead-width ratio, 316LSi was less likely to form IF defects within the build. This result suggests that 316LSi is more robust against process variations that can lead to defect formation and should be considered for use in structural applications. Furthermore, this work shows that more incipient IF defects are observed at the surface of a build than are retained in the build after subsequent layers. This finding suggests that in-situ thermography is very sensitive in detecting the precursors for IF defects in the build and can be employed for process monitoring and control for fracture-critical structural components. Finally, the overall lower stacking fault energy in 316LSi leads to smaller differences in deformation behavior based on loading direction, leading to more isotropic tensile properties. Although more work is needed to better understand the deformation and fracture characteristics of GMA-DED stainless steels, this work indicates that the combination of in-situ thermography and the use of 316LSi feedstocks should lead to the lowest occurrence of IF defects and the most isotropic tensile properties.

Conclusions

The influence of hatch spacing on tensile properties of high deposition rate GMA-DED of 316L and 316LSi were investigated by systematically changing the hatch-spacing-to-bead-width ratio to induce IF defects. Samples were taken parallel and perpendicular to the build direction and tested to evaluate the influence of IF defects at room temperature tensile properties. Based on the results, the following conclusions are made:

- Increases in hatch-spacing-to-bead-width ratio from 0.58 to 0.80 led to an increase in the size and frequency of IF defects in the builds. For a given hatch-spacing-to-bead-width ratio, 316LSi showed smaller and fewer IF defects compared to 316L, likely due to higher liquid fluidity.
- Incipient IF defects between deposition passes were more frequently observed at the top of the build using in-situ thermography than were observed in the build after subsequent passes, indicating that thermography can be employed as a sensitive quality control technique.
- With increasing hatch-spacing-to-bead-width ratio, the tensile properties of 316L responded non-monotonically, and the differences in tensile properties between horizontally and vertically loaded tensile samples appeared to be more strongly influenced by differences in crystallographic direction relative to the loading direction rather than the presence of IF defects.

■ 316LSi showed no statistically significant influences of hatch-spacing-to-bead-width ratio or loading direction on tensile properties, indicating that 316LSi is more robust to the evaluated process variations and should be considered for structural applications.

Acknowledgements

The authors acknowledge support from the Manufacturing and Materials Joining Innovation Center (Ma^{2}JIC), USA, a National Science Foundation Industry/University Cooperative Research Center (I/UCRC), USA, (Award No. 2052819) at the Colorado School of Mines (Mines), Golden, Colo. Data analysis was supported by instrumentation that was acquired through the support of the National Science Foundation (DMR-1828454).

Author Contributions

Dominic Piccone: Formal Analysis, Investigation, Writing – Original Draft, Writing – Review and Editing

Luc Hagen: Formal Analysis, Investigation, Writing – Original Draft, Writing – Review

Stephen Tate: Conceptualization, Resources, Writing – Review and Editing, Funding Acquisition

Jonah Klemm-Toole: Conceptualization, Methodology, Resources, Writing – Review and Editing, Supervision, Funding Acquisition

Conflict of Interest

On behalf of all authors, the corresponding author states that there is no conflict of interest.

References

1. Wu, B., et al. 2018. A review of the wire arc additive manufacturing of metals: properties, defects, and quality improvement. *Journal of Manufacturing Processes* 35: 127–139.

2. Lippold, J. C. 2014. *Welding Metallurgy and Weldability*. Hoboken, N.J.: John Wiley & Sons.

3. Tang, M., Pistorius, P. C., and Beuth, J. L. 2017. Prediction of lack-of-fusion porosity for powder bed fusion. *Additive Manufacturing* 14: 39–48.

4. Ding, D., et al. 2015. A multi-bead overlapping model for robotic wire and arc additive manufacturing (WAAM). *Robotics and Computer-Integrated Manufacturing* 31: 101–110.

5. Xu, X., et al. 2019. Preliminary investigation of building strategies of maraging steel bulk material using wire + arc additive manufacture. *Journal of Materials Engineering and Performance* 28: 594–600.

6. Ronneberg, T., Davies, C. M., and Hooper, P. A. 2020. Revealing relationships between porosity, microstructure, and mechanical properties of laser powder bed fusion 316L stainless steel through heat treatment. *Materials & Design* 189: 108481.

7. Prasad, R. G., et al. 2020. Influence of pore characteristics on anisotropic mechanical behavior of laser powder bed fusion–manufactured metal by micromechanical modeling. *Advanced Engineering Materials* 22(12): 2000641.

8. Wilson-Heid, A. E., Novak, T. C., and Beese, A. M. 2019. Characterization of the effects of internal pores on tensile properties of additively manufactured austenitic stainless steel 316L. *Experimental Mechanics* 59: 793–804.

9. Biswal, R., et al. 2019. Criticality of porosity defects on the fatigue performance of wire + arc additive manufactured titanium alloy. *International Journal of Fatigue* 122: 208–217.

10. Lincoln Electric. Blue Max® MIG 316L. Retrieved December 8, 2024, from *https://www.lincolnelectric.com/en/products/blumaxmig316l_gmaw.*

11. Lincoln Electric. Lincoln® Red Max® 316LSi. Retrieved December 8, 2024, from *https://www.lincolnelectric.com/en/products/lincolnredmax316lsi_gmaw.*

12. ASTM International Committee E-28 on Mechanical Testing. 2021. *Standard Test Methods for Tension Testing of Metallic Materials*. ASTM International.

13. Hagen, L., et al. 2023. High deposition rate wire-arc directed energy deposition of 316L and 316LSi: process exploration and modelling. *Materials Science and Engineering: A* 880: 145044.

14. DeNonno, O., et al. 2024. Solidification behavior and texture of 316L austenitic stainless steel by laser wire directed energy deposition. *Materials Characterization* 211: 113916.

15. Elmer, J. W., et al. 2020. Wire-based additive manufacturing of stainless steel components. *Welding Journal* 99(1): 8-s to 24-s.

16. Wang, L., Xue, J., and Wang, Q. 2019. Correlation between arc mode, microstructure, and mechanical properties during wire arc additive manufacturing of 316L stainless steel. *Materials Science and Engineering: A* 751: 183–190.

17. Wang, X., et al. 2019. Crystallographic-orientation-dependent tensile behaviors of stainless steel 316L fabricated by laser powder bed fusion. *Materials Science and Engineering: A* 766: 138395.

18. Yonezawa, T., et al. 2013. The effect of chemical composition and heat treatment conditions on stacking fault energy for Fe-Cr-Ni austenitic stainless steel. *Metallurgical and Materials Transactions A* 44: 5884–5896.

19. Molnar, D., et al. 2019. Effect of temperature on the stacking fault energy and deformation behavior in 316L austenitic stainless steel. *Materials Science and Engineering: A* 759: 490–497.

20. Andrade, D. G., et al. 2024. Mechanical properties of 3D printed CMT-WAAM 316 LSi stainless steel walls. *Journal of Constructional Steel Research* 215: 108527.

21. Schreiber, M., et al. 2024. Influence of annealing on microstructures and mechanical properties of laser powder bed fusion and wire arc directed energy deposition additively manufactured 316L. *Materials Science and Engineering: A* 917: 147390.

DOMINIC PICCONE, **LUC HAGEN**, and **JONAH KLEMM-TOOL** (*jklemmto@mines.edu*) are with the Colorado School of Mines, Golden, Colo. **STEPHEN TATE** is with the Electrical Power Research Institute, Charlotte, N.C.